JOURNAL OF SPACECRAFT AND ROCKETS
Vol. 44, No. 5, September–October 2007

Analytic Model of Catastrophic Yaw

J. Morote*
National Institute of Aerospace Technology, 28850 Madrid, Spain

DOI: 10.2514/1.29858

A quantitative model of the nonlinear motion leading to catastrophic yaw of finned missiles is presented. The coupled roll–yaw dynamics of the missile, acted on by the trim angle of attack due to slight configurational asymmetries, is represented by pitch, yaw, and roll equations of motion that include cubic aerodynamic coefficients and roll-orientation-dependent induced moments. The steady-state equilibrium points of the system are found and their stability is determined by linearization. The solutions are evaluated by comparison with numerical integration of the equations of motion, proving the capability of the model to predict catastrophic yaw.

Nomenclature

C_D	=	drag force coefficient
$C_{L\alpha}$	=	angle-of-attack coefficient of the lift force
$C_{M\alpha}$	=	angle-of-attack coefficient of the pitch moment
$C_{Mp\alpha}$	=	angle-of-attack coefficient of the Magnus moment
C_{Mq}, $C_{M\dot{\alpha}}$	=	damping and lag coefficients of the pitch moment
$C_{M0}e^{i\phi_{M0}}$	=	asymmetry moment coefficient
$C_{N\alpha}$	=	angle-of-attack coefficient of the normal force
$C_{N0}e^{i\phi_{N0}}$	=	asymmetry force coefficient
C^*	=	$C(\rho SD/2m)$
Cl_i	=	induced roll moment coefficient
Cl_p	=	roll damping moment coefficient
Cl_δ	=	roll effectiveness moment coefficient
D	=	reference length, missile diameter
I_x	=	axial moment of inertia
I_y	=	transversal moment of inertia
k_a	=	axial radii of gyration
k_t	=	transverse radii of gyration
m	=	mass
p	=	roll rate
q_d	=	dynamic pressure
$\hat{r}$	=	dimensionless radial offset of the center of mass
S	=	reference area, $\pi D^2/4$
s	=	dimensionless arc length
u	=	X component of velocity
V	=	speed of the missile
v	=	Y component of velocity
w	=	Z component of velocity
α, β	=	angles of attack and sideslip
γ	=	u/V
δ	=	magnitude of the complex angle of attack, $\tilde{\xi}$
δ_T	=	fin-cant angle
$\tilde{\mu}$	=	complex transverse angular velocity in nonrolling axes, $(\tilde{q} + i\tilde{r})D/V$
$\tilde{\xi}$	=	$\tilde{\beta} + i\tilde{\alpha}$ angle of attack in nonrolling axes, $(\tilde{u} + i\tilde{w})/V$
ξ_0	=	$\beta_0 + i\alpha_0$ static angle of attack in fixed axes at $p = 0$
σ	=	I_x/I_y
ϕ	=	roll angle
φ	=	phase lag

Subscripts

e	=	steady state
r	=	resonance

Superscripts

$\dot{}$	=	differentiation with respect to t
$\sim$	=	nonrolling axes

I. Introduction

FINNED projectiles, bombs, and unguided rockets occasionally exhibit abnormal flight behavior when experiencing large pitch–yaw angular motions and unintentionally spinning at a rate near the pitch frequency [1,2]. This comportment was attributed to the trim angle of attack originated by slight configurational asymmetries, which displays a peak amplification when the roll rate is near the pitch frequency [1]. The enlarged trim angle of attack causes an induced roll moment, nonlinear in both angle of attack and roll orientation, that under certain circumstances can lock the roll rate to the pitch frequency [1]. The *lock-in* of the two frequencies gives rise to a *lunar* [3] motion, allowing the action of a Magnus-type moment [the induced side moment, which (like the induced roll moment) is nonlinear in both angle of attack and roll orientation] that can reduce the yaw damping of the missile [4]. The resulting steady-state coupling between the rolling and the angular motions occasionally exhibits the large-amplitude oscillations characteristic of *catastrophic yaw* [3]. Linear nonrolling theory [5], which considers a missile with linear aerodynamic properties at a constant value of the rolling velocity, is capable of predicting the occurrence of roll resonance and the amplification of the trim angle at resonance. However, roll lock-in and catastrophic yaw are nonlinear in nature and require a nonlinear model for the coupled roll–yaw dynamics of the missile.

The effects of angle-of-attack and roll-orientation nonlinearities on the angular motion of missiles have been investigated [6–13]. Murphy [14] developed a fifth-order autonomous nonlinear system model for the long-term coupled roll–yaw motion of a missile, combining linear transverse aerodynamics and nonlinear roll aerodynamics. The nonlinear rolling motion was due to a roll-orientation-dependent induced roll moment caused by center-of-mass offset. This model has shown [14–16] the capability of predicting normal and reverse persistent resonance, quasi-steady roll lock-in and the existence of limit cycles, and has been extended [17] to include nonlinear transverse aerodynamic properties. The model could not demonstrate the phenomenon of catastrophic yaw because it lacks nonlinear induced side forces and yaw moments.

The roll-orientation-dependent nonlinear yaw moment is a Magnus-type moment, which (unlike the classical Magnus moment) acts perceptibly even at small roll rates. This moment has long been recognized [2] to be the origin of the large multiplying factors for the trim angle. In this paper, persistent resonance and catastrophic yaw

Presented as Paper 458 at the 45th AIAA Aerospace Sciences Meeting and Exhibit, Reno, NV, 8–11 January 2007; received 19 January 2007; revision received 30 April 2007; accepted for publication 3 June 2007.

*Research Engineer, Aerodynamics Branch, Instituto Nacional de Técnicas Aeroespaciales (INTA), Torrejón de Ardoz. Member AIAA.

are investigated with a nonlinear model of pitch–yaw motion, including a nonlinear induced yawing moment coupled to nonlinear rolling motion induced by configurational asymmetries. The equilibrium points of the steady-state motion are found graphically and their stability is determined by linearization about the solutions. The quantitative long-term behavior of the model is shown to be capable of exhibiting catastrophic yaw. Comparisons with three-degree-of-freedom simulations confirm the large-amplitude motions characteristic of catastrophic yaw.

II. Roll-Orientation-Dependent Equations of Motion

A. Lateral Motion

For a symmetric cruciform missile, the static normal force and restoring torque are functions of the angle of attack, but also vary with the orientation of the angle-of-attack plane with respect to the missile-fixed system of axes $\theta = \phi_{M0} - \varphi$ (Fig. 1). Given some assumptions concerning the fluid forces acting on a cruciform missile [18], the static force and moment expansions in nonrolling axes up to the lowest-order terms capable of discerning roll-orientation dependence are

$$\begin{aligned}\tilde{C}_y + i\tilde{C}_z|_{\text{static}} &= -(C_{N\alpha 0} + C_{N\alpha 2}\delta^2 + C_{N\theta 2}\delta^2 e^{-i4(\phi_{M0}-\varphi)})\tilde{\xi}\\ \tilde{C}_m + i\tilde{C}_n|_{\text{static}} &= -i(C_{M\alpha 0} + C_{M\alpha 2}\delta^2 + C_{M\theta 2}\delta^2 e^{-i4(\phi_{M0}-\varphi)})\tilde{\xi}\end{aligned} \tag{1}$$

The complex force and moment differential equations of rocket motion [6] written in terms of the complex angle of attack $\tilde{\xi}$ and the complex angular velocity $\tilde{\mu}$, disregarding gravity effects, are

$$\begin{aligned}\tilde{\xi}' - C_D^*\tilde{\xi} - i\gamma\mu &= \tilde{C}_y^* + i\tilde{C}_z^*\\ \tilde{\mu}' - C_D^*\tilde{\mu} - i\sigma\phi'\tilde{\mu} &= k_t^{-2}(\tilde{C}_m^* + i\tilde{C}_n^*)\end{aligned} \tag{2}$$

where the tilde superscript denotes differentiation with respect to the dimensionless arc length:

$$s = \int_{to}^{t} (V/D)\,\mathrm{d}t$$

Excluding the Magnus force and including quadratic drag force and cubic damping and lag and Magnus moments from Eqs. (2), the transverse equation of motion of a slightly asymmetric missile, assuming constant flight conditions and small geometrical angles, can be written as

$$\begin{aligned}&\tilde{\xi}'' + (H_0 + H_2\delta^2 - i\sigma\phi')\tilde{\xi}' - [M_0 + M_2\delta^2 + i\sigma\phi'(T_0 + T_2\delta^2)]\tilde{\xi}\\ &\quad = [M_R + N_R(i\phi'(\sigma - 4) - 2\bar{\tilde{\xi}}'/\bar{\tilde{\xi}} + \tilde{\xi}'/\tilde{\xi})]\delta^2 e^{-i4(\phi_{M0}-\varphi)}\tilde{\xi} + M_A e^{i\phi}\end{aligned} \tag{3}$$

where

$$\begin{aligned}H_i &= C_{N\alpha i}^* - 2C_{Di}^* - k_t^{-2}(C_{Mqi}^* + C_{M\dot{\alpha}i}^*) \qquad M_i = k_t^{-2}C_{M\alpha i}^*\\ T_i &= C_{N\alpha i}^* - C_{Di}^* + k_a^{-2}C_{Mp\alpha i}^* \qquad M_R = k_t^{-2}C_{M\theta 2}^* \qquad N_R = C_{N\theta 2}^*\\ M_A &= \frac{\rho SD^3}{2I_y}[C_{M0}e^{i\phi_{M0}} - ik_t^2(1-\sigma)\phi' C_{N0}e^{i\phi_{N0}}]\end{aligned}$$

The coefficients on the left side of the differential equation of motion in the complex angle of attack $\tilde{\xi}$ are functions of its size δ, and the roll-orientation-dependent aerodynamics are manifest by the right side of the equation. The revolving term in nonrolling axes that introduces the effect of small configurational asymmetries is represented by the term in M_A.

The roll-orientation-dependent normal force term can be neglected in comparison with the moment term, because N_R appears multiplied by ϕ' (on the order of 10^{-2}) and by the terms $\bar{\tilde{\xi}}'/\bar{\tilde{\xi}}$ and $\tilde{\xi}'/\tilde{\xi}$ that are proportional to the frequency of the yawing motion (on the order of 10^{-3}). The transverse equation of motion (3) can then be written as

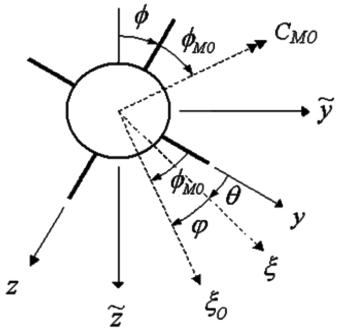

Fig. 1 Systems of axes.

$$\begin{aligned}&\tilde{\xi}'' + (H_0 + H_2\delta^2 - i\sigma\phi')\tilde{\xi}' - [M_0 + M_2\delta^2 + M_R\delta^2 e^{-i4(\phi_{M0}-\varphi)}\\ &\quad + i\sigma\phi'(T_0 + T_2\delta^2)]\tilde{\xi} = Fe^{i(\phi+\phi_{M0})}\end{aligned} \tag{4}$$

where the C_{N0} term in M_A was neglected because ϕ' is on the order of 10^{-2} and $F = (\rho SD^3/2I_y)C_{M0}$.

The nonrolling axes differ from the missile-fixed system of axes (Fig. 1) by the roll angle:

$$\phi = \int_{to}^{t} p\,\mathrm{d}t$$

$$\tilde{\xi} = \xi e^{i\phi} \tag{5}$$

Substitution of Eq. (5) into Eq. (4) yields the nonlinear lateral equation of motion in fixed axes that includes a roll-orientation-dependent Magnus-type moment, the imaginary part of the term in M_R:

$$\begin{aligned}&\xi'' + \xi'[H_0 + H_2\delta^2 + i\phi'(1+\tau)] - \xi\{\tau\phi'^2 + M_0 + M_2\delta^2\\ &\quad + M_R\delta^2 e^{-i4(\phi_{M0}-\varphi)} - i[\phi'' + \phi'(h_0 + h_2\delta^2)]\} = Fe^{i\phi_{M0}}\end{aligned} \tag{6}$$

where

$$h_i = H_i - \sigma T_i \qquad \tau = 1 - \sigma$$

B. Rolling Motion

The nonlinear rolling motion considered here is due to induced roll moments if the missile is not a body of revolution. The other two components are a constant driving moment due to differential cant of the fin surfaces and a damping component proportional to the roll rate. No additional nonlinearities were considered in the damping term [19,20].

$$I_x\dot{p} = q_d SD\left[Cl_\delta\delta_T + Cl_p\frac{pD}{V} + Cl_i\right] \tag{7}$$

By the use of dimensionless distance s as independent variable, Eq. (7) becomes

$$\phi'' + (K_{p0} + K_{p2}\delta^2)\phi' - K_\delta - K_i = 0 \tag{8}$$

where

$$\begin{aligned}K_{p0} &= -(C_{D0}^* + k_a^{-2}Cl_p^*) \qquad K_{p2} = -C_{D2}^*\\ K_\delta &= k_a^{-2}Cl_\delta^*\delta_T \qquad K_i = k_a^{-2}Cl_i^*\end{aligned}$$

Two sources of nonlinear induced roll moments Cl_i are considered in the model: the coupling of a lateral center-of-mass offset with the normal force associated with a trim angle and the cyclic fin loading on cruciform finned vehicles at angle of attack.

The roll moment caused by lateral offset of the center of mass (Fig. 2), in the presence of the normal force associated with a trim angle is

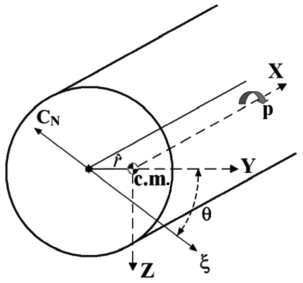

Fig. 2 Roll moment due to a lateral c.g. offset.

$$Cl_i = \hat{r}C_{N\alpha}\delta\sin\theta = \hat{r}(C_{N\alpha 0} + C_{N\alpha 2}\delta^2)\delta\sin\theta \tag{9}$$

where the term in $C_{N\theta 2}$ was disregarded.

The roll moment due to a cruciform tail is sinusoidal with the fin-orientation angle θ and nonlinear with the total angle of attack. Reference [21] provides an analytic form based on the experimental testing for the Aerobee rocket:

$$Cl_i = (C_{T0} + C_{T2}\delta^2)\delta\sin 4\theta \tag{10}$$

Neglecting nonzero cross products of inertia due to a small center-of-mass offset and assuming the induced roll moment to be the sum of the component due to the center-of-mass offset and the component due to the cruciform tail, the final form of the roll equation (8) is

$$\phi'' + (K_{p0} + K_{p2}\delta^2)\phi' - K_\delta - K_m(N_0 + N_2\delta^2)\delta\sin(\phi_{M0} - \varphi) - (K_{T0} + K_{T2}\delta^2)\delta\sin 4(\phi_{M0} - \varphi) = 0 \tag{11}$$

where

$$K_m = k_a^{-2}\hat{r} \qquad N_i = C^*_{N\alpha i} \qquad K_{Ti} = k_a^{-2}C^*_{Ti}$$

III. Long-Term Behavior

The long-term behavior of the system represented by Eqs. (6) and (11), when the transient motion has damped out, can head for some final equilibrium point, for the periodic motion represented by a limit cycle, or for the aperiodic behavior characteristic of chaotic motion. At roll lock-in, the missiles' rolling motion stays the same as the frequency of the wobbling motion [3]. Occasionally, the size of the wobbling motion is much larger than predicted by the linear theory, which is the phenomenon known as catastrophic yaw. Persistent resonance and catastrophic yaw are characterized by constant values of the roll rate and the angular amplitude of motion and are equilibrium points. Equilibrium points for the long-term behavior of the rocket, including the steady-state point set by the designer, are constant solutions of the nonlinear coupled system of equations (6) and (11) that can be transformed into a first-order system by taking $\xi' = \zeta$ and $\phi' = \omega$:

$$\zeta' + \xi'[H_0 + H_2\delta^2 + i\omega(1+\tau)] - \xi\{\tau\omega^2 + M_0 + M_2\delta^2 + M_R\delta^2 e^{-i4(\phi_{M0}-\varphi)} - i[\omega' + \omega(h_0 + h_2\delta^2)]\} = Fe^{i\phi_{M0}} \tag{12}$$

$$\zeta = \xi' \tag{13}$$

$$\omega' + (K_{p0} + K_{p2}\delta^2)\omega - K_\delta - K_m(N_0 + N_2\delta^2)\delta\sin(\phi_{M0} - \varphi) - (K_{T0} + K_{T2}\delta^2)\delta\sin 4(\phi_{M0} - \varphi) = 0 \tag{14}$$

where Eqs. (12) and (13) can be separated into real and imaginary parts and, consequently, the system can be cast as a system of five first-order coupled nonlinear differential equations.

The fixed or equilibrium points are found by setting all derivatives to zero, leading to the following system:

$$-\xi_e\{\tau\omega_e^2 + M_0 + M_2\delta_e^2 + M_R\delta_e^2 e^{-i4(\phi_{M0}-\varphi_e)} - i[\omega_e(h_0 + h_2\delta_e^2)]\} = Fe^{i\phi_{M0}} \tag{15}$$

$$\zeta_e = 0 \tag{16}$$

$$(K_{p0} + K_{p2}\delta_e^2)\omega_e - K_\delta - K_m(N_0 + N_2\delta_e^2)\delta_e\sin(\phi_{M0} - \varphi_e) - (K_{T0} + K_{T2}\delta_e^2)\delta_e\sin 4(\phi_{M0} - \varphi_e) = 0 \tag{17}$$

where the subscript e refers to steady-state conditions. Equation (16) states that the derivatives of the angles of attack and sideslip are zero at steady state and can be disregarded. Writing the complex angle of attack in polar coordinates $\xi = A\ e^{i(\phi_{M0}-\varphi)}$:

$$-A_e e^{-i\varphi_e}\{\tau\omega_e^2 + M_0 + M_2A_e^2 + M_RA_e^2 e^{-i4(\phi_{M0}-\varphi_e)} - i[\omega_e(h_0 + h_2A_e^2)]\} = F \tag{18}$$

$$(K_{p0} + K_{p2}A_e^2)\omega_e - K_\delta - K_m(N_0 + N_2A_e^2)A_e\sin(\phi_{M0} - \varphi_e) - (K_{T0} + K_{T2}A_e^2)A_e\sin 4(\phi_{M0} - \varphi_e) = 0 \tag{19}$$

The equilibrium points of the long-term behavior of the rocket are triads $(A_e, \omega_e, \varphi_e)$ that are simultaneously the solution of the steady-state lateral equation of motion (18) and the steady-state rolling equation of motion (19).

A. Steady-State Lateral Motion

Equation (18) can be separated into real and imaginary parts to give

$$A_e\lfloor\tau\omega_e^2 + M_0 + M_2A_e^2 + M_RA_e^2\cos 4(\phi_{M0} - \varphi_e)\rfloor = -F\cos\varphi_e \tag{20}$$

$$A_e\lfloor\omega_e(h_0 + h_2A_e^2) + M_RA_e^2\sin 4(\phi_{M0} - \varphi_e)\rfloor = F\sin\varphi_e \tag{21}$$

Equations (20) and (21) are two surfaces in the three-dimensional space $(A_e, \omega_e, \varphi_e)$, intersecting along a discontinuous curve, for which the points are possible solutions of the system of equations (18) and (19). The points $(A_e, \omega_e, \varphi_e)$ of the curve defined by Eqs. (20) and (21) can be found by writing the system as

$$\omega_e = \sqrt{-F\cos\varphi_e/A_e - M_0 - M_2A_e^2 - M_RA_e^2\cos 4(\phi_{M0} - \varphi_e)}/\tau$$

$$\omega_e = [F\sin\varphi_e/A_e - M_RA_e^2\sin 4(\phi_{M0} - \varphi_e)]/(h_0 + h_2A_e^2)$$

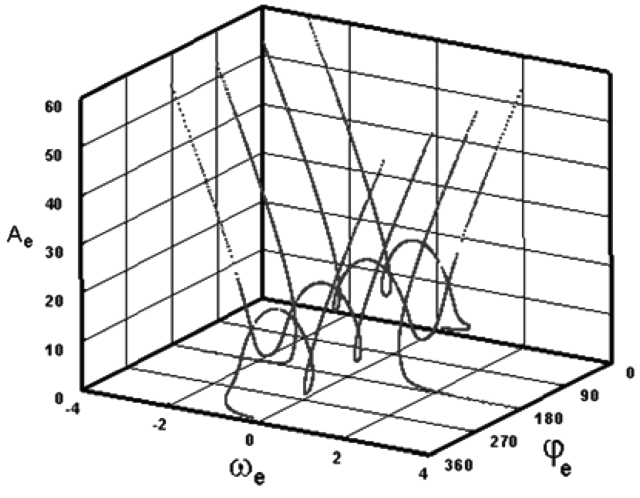

Fig. 3 Steady-state lateral equilibrium points.

Table 1 Parameters of Fig. 3

$M_0 = -4.61 \times 10^{-5}$	$k_t^{-2} = 0.053$
$M_R = -3.73 \times 10^{-4}$	$\rho SD/2m = 3.47 \times 10^{-5}$
$h_0 = 3.73 \times 10^{-4}$	$\tau = 0.96$

For a fine grid of values A_e and φ_e inside a given range, if the difference between the values of ω_e obtained from the two former expressions is less than a preset small ϵ, the corresponding triad $(A_e, \omega_e, \varphi_e)$ is taken as a solution of the system. Figure 3 shows the curve intersection of Eqs. (20) and (21) for a case in which the static trim angle is 1 deg and the nonlinear damping and static restoring torque, h_2 and M_2, were set to zero and $\phi_{M0} = 90$ deg, respectively. The rest of the parameters used in the calculations appear in Table 1.

The amplitude and phase are expressed in degrees, whereas the roll rates were scaled by the linear frequency of resonance [1]: $\omega_r \approx \sqrt{-M_0/\tau}$. The range of exploration looking for solutions of the system was $A_e \in [0, 60\,\text{deg}]$ and $\varphi_e \in [0, 360\,\text{deg}]$, with a grid of $(6 \times 10^4) \times (6 \times 10^4)$ points. The value of $\epsilon$was 1.5×10^{-6}, yielding 98,324 triad $(A_e, \omega_e, \varphi_e)$ solutions of the system.

For comparison purposes, Fig. 4 shows the projection of the curve of Fig. 3 onto the A_e–ω_e plane following the removal of lateral equilibrium points corresponding to negative roll rates and those in the interval of $\varphi_e \in [180, 360\,\text{deg}]$. The same figure depicts the nonlinear roll-orientation-independent ($M_2 = -6.59 \times 10^{-4}$, $M_R = 0$) and linear ($M_2 = M_R = 0$) projections of the corresponding three-dimensional curves, keeping the rest of the parameters the same.

Two characteristics stand out: First, the presence of the term in M_R in Eq. (21) makes possible the existence of very large amplitudes simultaneously being the solution of Eqs. (20) and (21). Assuming $h_2 = 0$ ($M_R = 0$), the steady-state amplitude allowed by Eq. (21) is $A_e = F \sin\varphi_e / \omega_e h_0$ and its maximum value is limited by the amount of damping in the system (h_0) for a given size of the asymmetry (F). Unfortunately, in the roll-orientation-dependent case, the steady-state amplitude from Eq. (21) is now given by $A_e = F \sin\varphi_e / [\omega_e h_0 + M_R A_e^2 \sin 4(\phi_{M0} - \varphi_e)]$, and the denominator can be very small for very large values of the amplitude in the left and right sides of the equation if the steady-state value of $\sin 4(\phi_{M0} - \varphi)$ is close to zero. Second, the single amplitude lobe of the two roll-orientation-independent curves ($M_R = 0$) appears divided into two tongues for the roll-orientation-dependent case ($M_R \neq 0$). This previously unexpected feature can be explained by the projection of the roll-orientation-dependent curve of Fig. 3 onto the φ_e–ω_e plane depicted in Fig. 5a, together with the amplitude-spin projection of Fig. 4, identifying the corresponding sections. The phase lag of the points on the left tongue of Fig. 5b for $\omega_e < 0.9$ are nearly 45 deg for the lower and 135 deg for the upper branch, respectively. With $M_R < 0$, the sign of the M_R term in Eq. (20) for these roll rates is positive, acting as a "soft-spring" restoring torque that bends the amplitude lobe to the left. For values of the scaled roll rate slightly above one, the phases on the right tongue are nearly 90 deg for the upper and 180 deg for the lower branch, respectively. The sign of the M_R term in Eq. (20) is now negative, acting as a "hard-spring" restoring torque that bends the amplitude lobe to the right. The effect of M_2 superimposed to M_R is to bend the whole scheme to the left for $M_2 > 0$ and to the right for $M_2 < 0$.

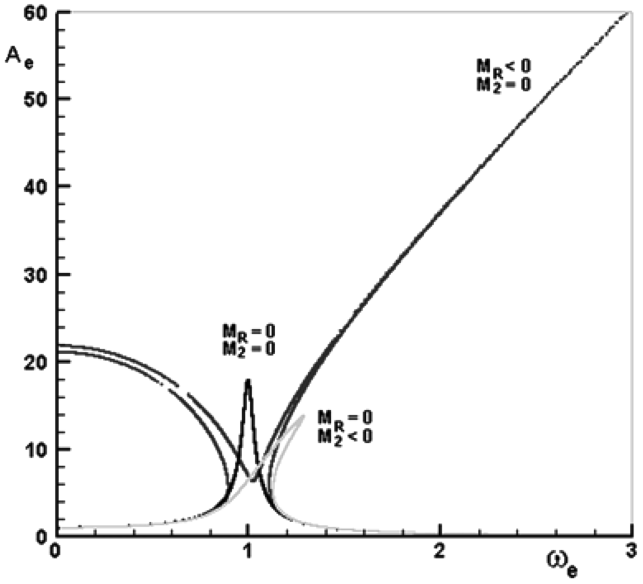

Fig. 4 Amplitude-spin projections.

B. Steady-State Rolling Motion and Equilibrium Points

The steady-state rolling equation of motion (19) is a surface in the three-dimensional space $(A_e, \omega_e, \varphi_e)$, for which the intersection with the curve defined by Eqs. (20) and (21) yields the equilibrium points. The steady-state equilibrium points of the system may be obtained graphically by writing Eq. (19) as

$$(K_{p0} + K_{p2}A_e^2)\omega_e - K_\delta = K_m(N_0 + N_2 A_e^2)A_e \sin(\phi_{M0} - \varphi_e) + (K_{T0} + K_{T2}A_e^2)A_e \sin 4(\phi_{M0} - \varphi_e) \tag{22}$$

and finding the intersections between the curves of the left- and the right-hand sides of Eq. (22) when the triad $(A_e, \omega_e, \varphi_e)$ solutions of the curve defined by Eqs. (20) and (21) are substituted on both sides of the equation.

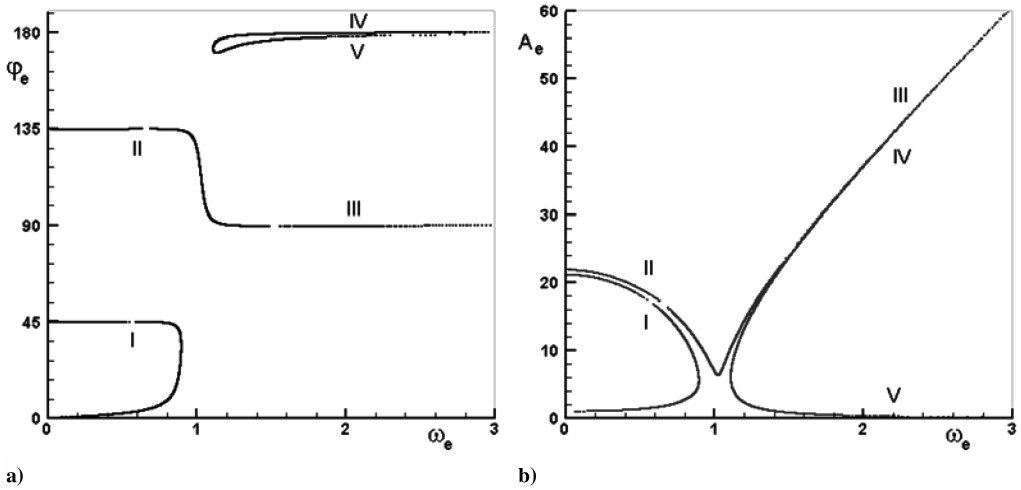

a) b)

Fig. 5 Phase-spin and amplitude-spin projections.

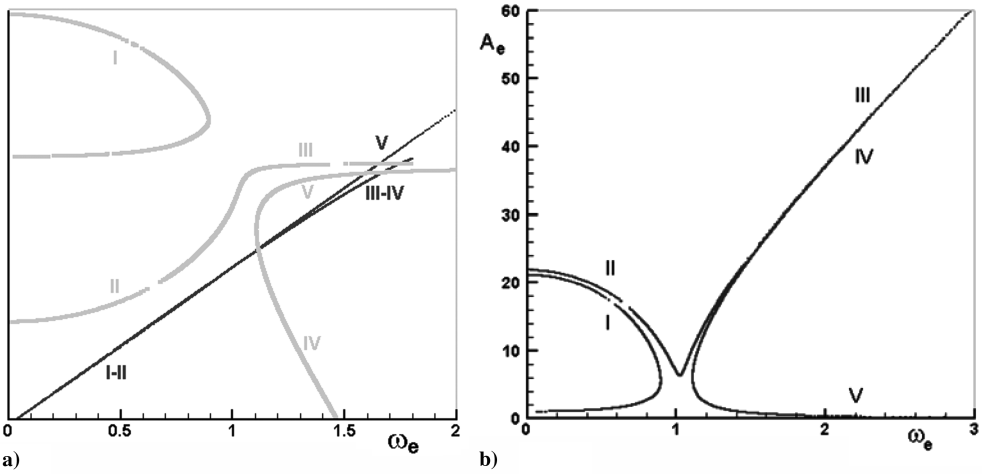

Fig. 6 Equilibrium points and amplitude-spin projection.

Figure 6a shows the two sides of Eq. (22) evaluated at the triad $(A_e, \omega_e, \varphi_e)$, with $K_{Ti} = 0$ for the roll-orientation-dependent case of Figs. 4 and 5, together with the amplitude-spin projection of Fig. 5b identifying corresponding sections. The rest of the parameters used in the calculations appear in Table 2.

The left side of Eq. (22) (black color in Fig. 6a) is nearly a straight line, with the exception of the frequency range of large amplitudes at which the line bifurcates due to the term in K_{p2}. The section that remains aligned corresponds to the small-amplitude section of Fig. 6b for roll rates above $\omega_e \approx 1.2$. The right side of Eq. (22) (gray color in Fig. 6a) presents the corresponding sections of Fig. 6b. The steady-state points of the system are the three intersecting points of the corresponding sections on the black and gray lines. The fin-cant term K_δ yields the intersecting point of the black line on the ordinate and can be set by the designer to intersect the gray curve at any given point by shifting up or down the black line. The difference between the right and left sides of the equation can be interpreted as the driving roll acceleration ω' that is zero at the equilibrium points. Figure 7 shows the driving roll acceleration corresponding to Fig. 6a, in which the three equilibrium points occur at the crossings with the zero line. The same figure presents the amplitude-spin projection of Fig. 6b in the right vertical-axis scale. The dashed lines show the position of the equilibrium points on the amplitude-spin curve. The steady-state solution for scaled roll rate $\omega_e = 2.8$ corresponds to an equilibrium solution (point 1) of very large amplitude.

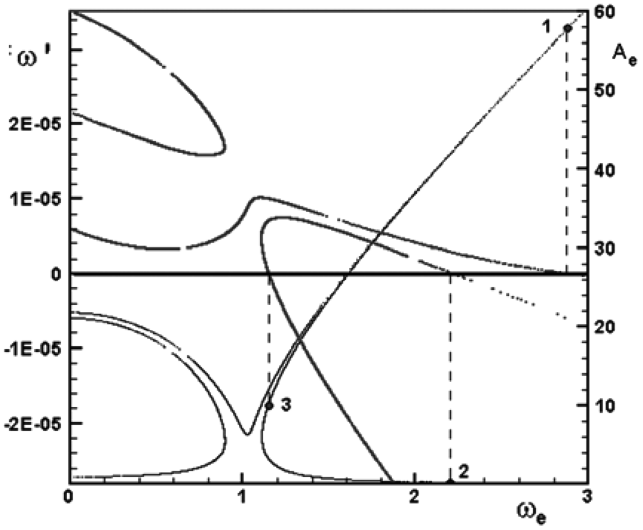

Fig. 7 Equilibrium points.

IV. Catastrophic Yaw

The previous section showed that the presence of the induced yaw moment M_R makes possible the existence of equilibrium points of very large amplitude. Should these solutions be stable, they represent the catastrophic yaw motion described by Nicolaides [2,3].

The coupled roll–yaw model of motion presented in this paper yields the long-term equilibrium points of the system, either the intended steady-state spin set by the designer (e.g., point 2 of Fig. 7) to reduce dispersion at a comfortable low-amplitude motion or equilibrium spins associated with motions from moderate (point 3 of Fig. 7) to very large amplitude (point 1 of Fig. 7). The equilibrium spin attained in a given flight requires the corresponding steady-state point to be stable, and for cases in which there are multiple stable equilibrium points, the initial conditions determine which one actually occurs. The stability analysis of the equilibrium points made in Appendix A shows that only the equilibrium point 2 of Fig. 7 is stable, and so this is the only long-term possible behavior of the case. Catastrophic yaw occurs when the long-term motion settles on a stable steady-state point associated with large-amplitude motion on the left or right tongues of the amplitude-spin curve.

Table 2 Parameters of Fig. 6

$K_{p0} = 1.32 \times 10^{-3}$	$N_0 = 2.74 \times 10^{-4}$
$K_{p2} = -2.74 \times 10^{-4}$	$N_2 = 0$
$K_\delta = 1.96 \times 10^{-5}$	$K_m = 0.2$

Figure 8 presents two cases in which there is one stable point of large amplitude. The presence of a hard-spring nonlinear restoring torque ($M_2 < 0$) bends the amplitude-spin curve to the right. Because every point $(A_e, \omega_e, \varphi_e)$ represented on the curve can be the equilibrium point of the case by properly setting K_δ, the stability analysis (see Appendix A) can be performed along the curve yielding its stable sections. The light gray color in Fig. 8 indicates the sections made up of potentially stable equilibrium points; that is, points that can be the stable equilibrium points of the case upon intersection with the zero line of Fig. 8b.

The figure includes the projections of numerical trajectories depicted with thin black lines and obtained from numerical simulation of Eqs. (6) and (11). The numerical simulations were performed with a fourth-order Runge–Kutta integration routine with a step size of $\Delta s = 0.1$. The parameters used for the calculations of the case of Fig. 8 appear in Table 3.

Figure 8a presents the projections of two numerical simulations converging toward two stable steady-state points on the amplitude-spin plot: trajectory A with initial conditions $\beta = 2$ deg, $\alpha = -1$ deg, $\dot{\beta} = 0$, $\dot{\alpha} = 0$, and $\phi' = 3$ and trajectory B with initial conditions $\beta = 3$ deg, $\alpha = -1$ deg, $\dot{\beta} = 0, \dot{\alpha} = 0$, and $\phi' = 3$. Trajectory A ends

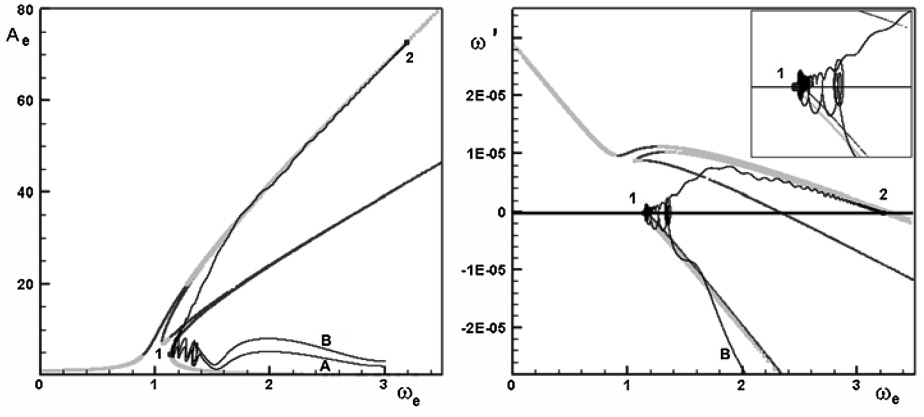

a) Amplitude spin b) Driving roll acceleration spin

Fig. 8 Catastrophic yaw (point 2).

at point 1 with 5 deg of amplitude at equilibrium. Trajectory B, as projected on the A_e–ω_e plane, mimics the first part of trajectory A and lingers in the neighborhood of the equilibrium point 1, finally heading for point 2 with 73 deg of amplitude at equilibrium. During the last part of the transient, the spin changes according to the degree of bending of the tongue and the total angle of attack builds up to a large value at equilibrium. The trajectories A and B end at the points 1 and 2 that are the equilibrium points predicted in Fig. 8b. The trajectory A has not been depicted in Fig. 8b, for clarity reasons. The upper-right corner of the figure shows a zoom of the proximities of the equilibrium point 1.

The case depicted in Fig. 8 is a very special case in which the equilibrium point of moderate amplitude (point 1) occurs at the border of one of the stable sections of the curve and for which at least one of the eigenvalues determining the stability of the point has a negative real part very to close to zero. The border between the basins of attraction of points 1 and 2 goes through the starting points of trajectories A and B, and the slight difference in the initial conditions causes trajectories A and B to end at different points. If the zero line of Fig. 8b shifts down by increasing the deflection in roll, then the intersecting point of moderate amplitude (point 1) moves away from the proximities of $\omega_e \approx 1$ to higher spins. The intersection now occurs clearly inside the stable section of the curve and there is still one stable equilibrium point of large amplitude (point 2), but all trajectories end at the point of low amplitude. Only when considering initial conditions of large amplitude, the trajectory ends at the point of large amplitude. Now the border between the basins of attraction of the points of low and large amplitude is in the region of large amplitudes.

Figure 9 shows the zone of Fig. 8b that should be avoided by proper selection of the fin-cant deflection to set the zero line. Inside this zone, the zero line would yield equilibrium spins $\omega_e \approx 1$ if linear aerodynamics were considered. For linear aerodynamics, the driving roll acceleration is just the straight line $\omega' = -K_{p0}\omega_e + K_\delta$, and the segment of circles is a good approximation to this line inside the zone. Here, catastrophic yaw can take place for initial conditions of small amplitude and lateral rates.

Figure 10 shows the amplitude of trajectories A and B of Fig. 8 in terms of the dimensionless arc length.

Figure 11 shows a case in which the zero line is again located inside the prohibited zone that would yield low-amplitude points in the proximities of $\omega_e \approx 1$ if linear aerodynamics were considered but equilibrium points of large amplitude occur instead. The parameters of the case of Fig. 11 are the same as those of Fig. 8,

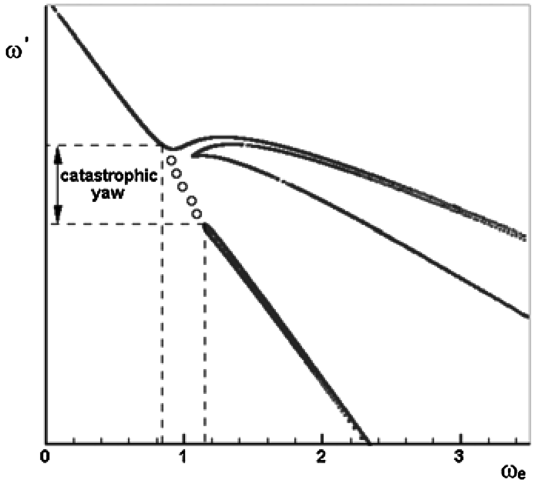

Fig. 9 Zone of possible catastrophic yaw.

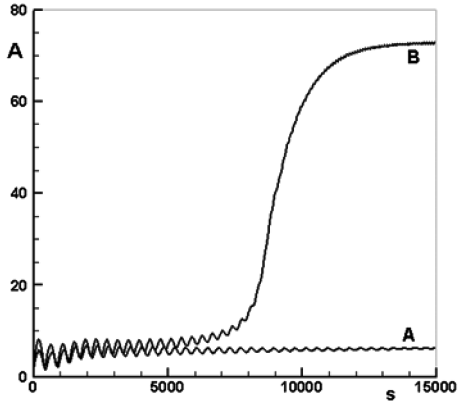

Fig. 10 Amplitude-arc length trajectories.

with the exception of $K_\delta = 2.10 \times 10^{-5}$ $N_2 = 5.75 \times 10^{-3}$ and $h_2 = 5.32 \times 10^{-3}$. In this case, there are only stable equilibrium points of large amplitude. The two equilibrium points are located on the left tongue of the amplitude-spin curve of Fig. 11a. The situation

Table 3 Parameters of Fig. 8

$M_0 = -4.61 \times 10^{-5}$	$h_0 = 3.73 \times 10^{-4}$	$K_{p0} = 3.50 \times 10^{-3}$	$N_0 = 2.74 \times 10^{-4}$	$\phi_{M0} = 145\,\text{deg}$
$M_2 = -5.27 \times 10^{-4}$	$h_2 = 0$	$K_{p2} = -2.74 \times 10^{-4}$	$N_2 = 0$	$k_i^{-2} = 0.053$
$M_R = -2.63 \times 10^{-4}$	$\tau = 0.96$	$K_\delta = 2.70 \times 10^{-5}$	$K_m = 0.2$	$\rho SD/2m = 3.47 \times 10^{-5}$

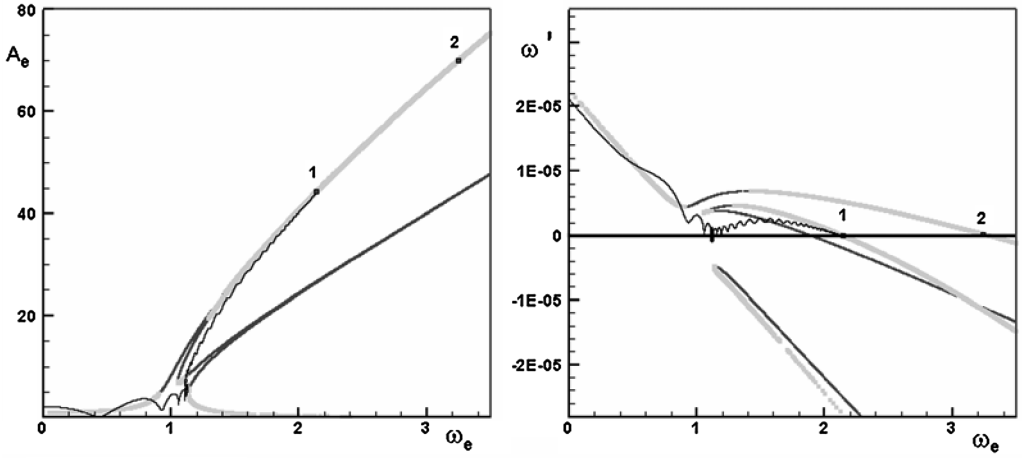

a) Amplitude spin **b) Driving roll acceleration spin**

Fig. 11 Catastrophic yaw (point 1).

of the equilibrium points of the case is determined in the ω' vs ω_e plot of Fig. 11b. The figures include the projections of a numerical trajectory with initial conditions $\beta = 2\,\text{deg}$, $\alpha = -1\,\text{deg}$, $\dot{\beta} = 0$, $\dot{\alpha} = 0$, and $\phi' = 0$ ending at point 1.

V. Conclusions

This paper presents a quantitative nonlinear roll–yaw dynamic model of long-term rocket motion capable of predicting catastrophic yaw. The model gives an insight into the mechanics of the induced yaw moment and shows quantitatively that the presence of the roll-orientation-dependent induced side moment can give rise to long-term equilibrium points of very large amplitude. The rest of the nonlinearities included in the model do not alter the existence of large-amplitude equilibrium points, but are significant in terms of their location and stability. According to the present model, catastrophic yaw would be an infrequent phenomenon consequence of an unusually large disturbance at release or the result of an unfortunate selection of a roll deflection that would yield steady-state spins near one, associated with low-amplitude motions in the linear case, when, in fact, the amplitude of the equilibrium points actually goes from moderate to very large. A systematic investigation of the influence of the aerodynamic properties to destabilize large-amplitude points should, it is hoped, provide useful design guidelines to eliminate the risk of occurrence of this flight condition, because the coexistence of stable solutions of small and large amplitude allows certain initial conditions to fall inside the basin of attraction of the stable point of large amplitude.

Appendix A: Stability of the Solutions

The stability of the steady-state solutions is obtained by linearizing about the equilibrium points of the equations of motion: the transverse equation of motion (6) and the roll equation (11):

$$\xi'' + \xi'[H_0 + H_2\delta^2 + i\omega(1+\tau)] - \xi\{\tau\omega^2 + M_0 + M_2\delta^2 + M_R\delta^2 e^{-i4(\phi_{M0}-\varphi)} - i[\omega' + \omega(h_0 + h_2\delta^2)]\} = Fe^{i\phi_{M0}} \tag{A1}$$

$$\omega' + (K_{p0} + K_{p2}\delta^2)\omega - K_\delta - K_m(N_0 + N_2\delta^2)\delta\sin(\phi_{M0} - \varphi) - (K_{T0} + K_{T2}\delta^2)\delta\sin 4(\phi_{M0} - \varphi) = 0 \tag{A2}$$

where ϕ' was replaced by ω. If a variational state due to a slight change in the initial conditions is considered and, accordingly, the two variables of the system, ξ and ω and the related δ and φ, are replaced by $\xi + \partial\xi$, $\omega + \partial\omega$, $\delta + \partial\delta$, and $\varphi + \partial\varphi$, respectively, and the variation powers above the first are neglected, then Eq. (A1) transforms to

$$\begin{aligned}&\partial\xi'' + \partial\xi'[H_0 + H_2\delta^2 + i\omega(1+\tau)] - \partial\xi\{\tau\omega^2 + M_0 + M_2\delta^2 \\ &\quad + M_R\delta^2 e^{-i4\theta} - i[\omega' + \omega(h_0 + h_2\delta^2)]\} + \partial\omega' i\xi \\ &\quad - \partial\omega\{2\tau\xi\omega - i[\xi'(1+\tau) + \xi(h_0 + h_2\delta^2)]\} \\ &\quad + \partial\delta 2\delta[\xi' H_2 - \xi M_2 - \xi M_R e^{-i4\theta} + i\xi h_2\omega] \\ &\quad - i4\xi M_R\delta^2 e^{-i4\theta}\partial\varphi = 0\end{aligned} \tag{A3}$$

where $\theta = \phi_{M0} - \varphi$.

By writing the complex angle of attack in polar coordinates $\xi = A\,e^{i(\phi_{M0}-\varphi)}$, particularizing for the steady-state point under investigation ($A = A_e$, $\omega = \omega_e$, and $\varphi = \varphi_e$) and introducing Eq. (18), Eq. (A3) transforms to

$$\begin{aligned}&(\partial A'' - iA_e\partial\varphi'') + (\partial A' - iA_e\partial\varphi')[H_0 + H_2A_e^2 + i\omega_e(1+\tau)] \\ &\quad + (\partial A - iA_e\partial\varphi)\frac{F}{A_e}e^{i\varphi_e} + \partial\omega' iA_e \\ &\quad - \partial\omega A_e[2\tau\omega_e - i(h_0 + h_2A_e^2)] \\ &\quad + \partial A 2A_e^2[-M_2 - M_R e^{-i4\theta_e} + ih_2\omega_e] \\ &\quad - i4M_R A_e^3 e^{-i4\theta_e}\partial\varphi = 0\end{aligned} \tag{A4}$$

where $\theta_e = \phi_{M0} - \varphi_e$. Similarly, the variational state of Eq. (A2) yields

$$\begin{aligned}&\partial\omega' + \partial\omega(K_{p0} + K_{p2}A_e^2) - \partial A[K_m(N_0 + 3N_2A_e^2)\sin\theta_e \\ &\quad + (K_{T0} + 3K_{T2}A_e^2)\sin 4\theta_e - 2K_{p2}A_e\omega_e] \\ &\quad + \partial\varphi A_e[K_m(N_0 + N_2A_e^2)\cos\theta_e \\ &\quad + 4(K_{T0} + K_{T2}A_e^2)\cos 4\theta_e] = 0\end{aligned} \tag{A5}$$

By now introducing $\partial\psi = A_e\partial\varphi$ and $\partial\varpi = A_e\partial\omega$, Eqs. (A4) and (A5) can be written as

$$\begin{aligned}&(\partial A'' - i\partial\psi'') + (\partial A' - i\partial\psi')[H_0 + H_2A_e^2 + i\omega_e(1+\tau)] \\ &\quad + (\partial A - i\partial\psi)\frac{F}{A_e}e^{i\varphi_e} + i\partial\varpi' - \partial\varpi[2\tau\omega_e - i(h_0 + h_2A_e^2)] \\ &\quad + \partial A 2A_e^2[-M_2 - M_R e^{-i4\theta_e} + ih_2\omega_e] - i4M_R A_e^2 e^{-i4\theta_e}\partial\psi = 0\end{aligned} \tag{A6}$$

Table A1 *Jf* matrix elements

$Jf_{11}=0$	$Jf_{12}=0$	$Jf_{13}=1$	$Jf_{14}=0$	$Jf_{15}=0$
$Jf_{21}=0$	$Jf_{22}=0$	$Jf_{23}=0$	$Jf_{24}=1$	$Jf_{25}=0$
$Jf_{31}=2A_e^2(M_2+M_R\cos 4\theta_e)-(F/A_e)\cos\varphi_e$	$Jf_{32}=4M_RA_e^2\sin 4\theta_e-(F/A_e)\sin\varphi_e$	$Jf_{33}=-(H_0+H_2A_e^2)$	$Jf_{34}=-\omega_e(1+\tau)$	$Jf_{35}=2\tau\omega_e$
$Jf_{41}=(F/A_e)\sin\varphi_e-2K_{p2}A_e^2\omega_e+$ $2A_e^2(\omega_eh_2+M_R\sin 4\theta_e)+K_mA_e(N_0+3N_2A_e^2)\sin\theta_e+$ $A_e(K_{T0}+3K_{T2}A_e^2)\sin 4\theta_e$	$Jf_{42}=-(F/A_e)\cos\varphi_e-K_mA_e(N_0+N_2A_e^2)\cos\theta_e-$ $4A_e(K_{T0}+K_{T2}A_e^2)\cos 4\theta_e-4M_RA_e^2\cos 4\theta_e$	$Jf_{43}=\omega_e(1+\tau)$	$Jf_{44}=-(H_0+H_2A_e^2)$	$Jf_{45}=h_0-K_{p0}+(h_2-K_{p2})A_e^2$
$Jf_{51}=K_mA_e(N_0+3N_2A_e^2)\sin\theta_e+$ $A_e(K_{T0}+3K_{T2}A_e^2)\sin 4\theta_e-2K_{p2}A_e^2\omega_e$	$Jf_{52}=-K_mA_e(N_0+N_2A_e^2)\cos\theta_e-4A_e(K_{T0}+K_{T2}A_e^2)\cos 4\theta_e$	$Jf_{53}=0$	$Jf_{54}=0$	$Jf_{55}=-(K_{p0}+K_{p2}A_e^2)$

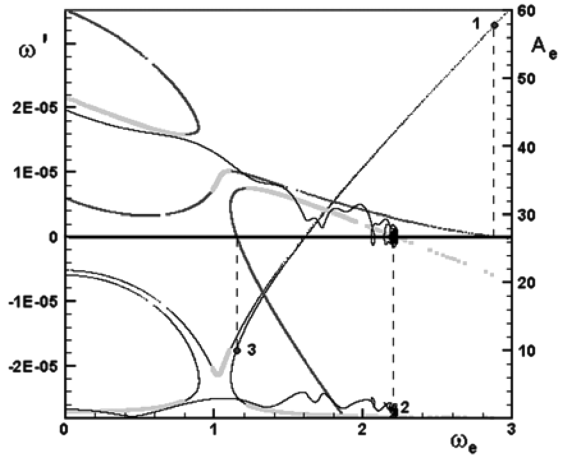

Fig. A1 Stable–unstable branches.

$$\partial\varpi' + \partial\varpi(K_{p0}+K_{p2}A_e^2) - \partial AA_e[K_m(N_0+3N_2A_e^2)\sin\theta_e + (K_{T0}+3K_{T2}A_e^2)\sin 4\theta_e - 2K_{p2}A_e\omega_e] + \partial\psi A_e[K_m(N_0+N_2A_e^2)\cos\theta_e + 4(K_{T0}+K_{T2}A_e^2)\cos 4\theta_e] = 0 \tag{A7}$$

Equations (A6) and (A7) describe the linearized behavior of the variations in the neighborhood of the equilibrium points $(A_e, \omega_e, \varphi_e)$ that can be expressed in state-space form as a system of five first-order linear differential equations:

$$\begin{bmatrix} \partial A' \\ \partial\psi' \\ \partial A'_{\text{tilde}} \\ \partial\psi'_{\text{tilde}} \\ \partial\varpi' \end{bmatrix} = [Jf] \begin{bmatrix} \partial A \\ \partial\psi \\ \partial A_{\text{tilde}} \\ \partial\psi_{\text{tilde}} \\ \partial\varpi \end{bmatrix} \tag{A8}$$

where $\partial A_{\text{tilde}} = \partial A'$ and $\partial\psi_{\text{tilde}} = \partial\psi'$ and the elements of $[Jf]$ are listed in Table A1.

The stability of the solution requires that all variations remain bounded for $s > 0$; otherwise, the point is unstable. This condition is satisfied if the eigenvalues of matrix Jf have negative real parts. The characteristic equation is a fifth-order polynomial equation for which the roots are the eigenvalues of matrix Jf. The search for the eigenvalues of the system (for every possible steady-state point $(A_e, \omega_e, \varphi_e)$ that can be reached by setting K_δ) is performed by standard library software and the signs of their real parts are evaluated, yielding the stable–unstable branches of the system. Figure A1 depicts (in light gray color) the stable sections of the curves of Fig. 7 (i.e., the locus of points on the curves for which all five eigenvalues have negative real parts). According to the figure, only the equilibrium point 2 is stable. The figure includes two projections of the same numerical trajectory with initial conditions $\beta = 1$ deg, $\alpha = 1$ deg, $\dot\beta = 0$, $\dot\alpha = 0$, and $\phi' = 0$ converging to the single stable point.

References

[1] Nicolaides, J. D., "On the Free Flight Motion of Missiles Having Slight Configurational Asymmetries," Inst. of Aeronautical Sciences, Rept. 395, 1952.

[2] Nicolaides, J. D., "Two Non-Linear Problems in the Flight Dynamics of Modern Ballistic Missiles," Inst. of Aeronautical Sciences, Rept. 59-17, 1959.

[3] Nicolaides, J. D., and Clare, T. A., "Nonlinear Resonance Instability in the Flight Dynamics of Missiles," AIAA Paper 70-969, 1970.

[4] Nicolaides, J. D., "A Review of Some recent Progress in Understanding Catastrophic Yaw," AGARD, Rept. 551, 1966.

[5] Nicolaides, J. D., *Free Flight Dynamics*, Aero-Space and Mechanical Engineering Dept., Univ. of Notre Dame, Notre Dame, IN, 1961.

[6] Murphy, C. H., "Free Flight Motion of Symmetric Missiles," Ballistic Research Lab., Rept. 1216, Aberdeen Proving Ground, MD, Mar. 1963.
[7] Murphy, C. H., "The Measurements of Non-Linear Forces and Moments by Means of Free Flight Test," Ballistic Research Lab., Rept. 974, Aberdeen Proving Ground, MD, 1956.
[8] Murphy, C. H., "The Effect of Strongly Non-Linear Static Moment on the Combined Pitching and Yawing Motion of a Symmetric Missile," Ballistic Research Lab., Rept. 1114, Aberdeen Proving Ground, MD, 1960.
[9] Nayfeh, A. H., "A Multiple Time Scaling Analysis of Reentry Roll Dynamics," *AIAA Journal*, Vol. 7, No. 10, 1969, pp. 2155–2157.
[10] Murphy, C. H., "Nonlinear Motion of a Missile with Slight Configurational Asymmetries," *Journal of Spacecraft and Rockets*, Vol. 8, No. 3, Mar. 1971, pp. 259–263.
[11] Clare, T. A., "Resonance Instability for Finned Configurations Having Nonlinear Aerodynamic Properties," *Journal of Spacecraft and Rockets*, Vol. 8, No. 3, 1971, pp. 278–283.
[12] Pepitone, T. R., "Resonant Behavior of a Symmetric Missile Having Roll Orientation-Dependent Aerodynamics," *Journal of Guidance and Control*, Vol. 1, No. 5, 1978, pp. 335–339.
[13] Pepitone, T. R., "The Influence of Roll Orientation-Dependent Aerodynamics on the Stability of Cruciform Missile Configuration," Naval Surface Weapons Center, Rept. NSWC/TR-79-416, Dalhgren, VA, 1979.
[14] Murphy, C. H., "Some Special Cases of Spin-Yaw Lock-In," *Journal of Guidance, Control, and Dynamics*, Vol. 12, No. 6, 1989, pp. 771–776.
[15] Ananthkrishnan, N., and Raisinghani, S. C., "Steady and Quasi-Steady Resonant Lock-In of Finned Projectiles," *Journal of Spacecraft and Rockets*, Vol. 29, No. 5, 1992, pp. 692–696.
[16] Tanrikulu, O., "Limit Cycle and Chaotic Behavior in Persistent Resonance of Unguided Missiles," *Journal of Spacecraft and Rockets*, Vol. 36, No. 6, 1999, pp. 859–865.
[17] Morote, J., "Resonant Lock-In of Unguided Rockets Having Non-Linear Aerodynamic Properties," AIAA Paper 2006-830, 2006.
[18] Maple, C. G., and Synge, J. L., "Aerodynamic Symmetry of Projectiles," *Quarterly of Applied Mathematics*, Vol. 4, Jan. 1949, pp. 345–366.
[19] Daniels, P., "A Study of the Nonlinear Rolling Motion of a Four-Finned Missile," *Journal of Spacecraft and Rockets*, Vol. 7, No. 4, 1970, pp. 510–512.
[20] Cohen, C., Clare, T., A., and Stevens, F. L., "Analysis of the Nonlinear Rolling Motion of Finned Missiles," *AIAA Journal*, Vol. 12, No. 3, 1974, pp. 303–309.
[21] Clare, T. A., "Non-Linear Resonance Instability in the Flight Dynamics of Missiles," Ph.D. Dissertation, Dept. of Aerospace and Mechanical Engineering, Univ. of Notre Dame, Notre Dame, IN, June 1970; Vol. 8, No. 3, 1971, pp. 278–283.

M. Costello
Associate Editor